Received: 16 May 2022 | Accepted: 19 May 2022

DOI: 10.1002/nano.202200102

RESEARCH ARTICLE

nano select Open Access WILEY

Microfluidic device with a carbonate-rich hydroxyapatite micro-coating

Florence H. Y. Lui[1] | **Liangcheng Xu**[2] | **Pierrette Michaux**[3] | **Joanna Biazik**[4] | **Gregory F. S. Harm**[4] | **Rema A. Oliver**[5] | **Pramod Koshy**[1] | **William R. Walsh**[5] | **Ralph J. Mobbs**[6] | **Tara C. Brennan-Speranza**[7] | **Yu Wang**[8] | **Lidan You**[2,9] | **Charles C. Sorrell**[1]

[1]School of Materials Science and Engineering, UNSW Sydney, Sydney, New South Wales, Australia

[2]Institute of Biomedical Engineering, University of Toronto, Toronto, Ontario, Canada

[3]Australian National Fabrication Facility (NSW Node), School of Physics, UNSW Sydney, Sydney, New South Wales, Australia

[4]Mark Wainwright Cell Culture Facility, UNSW Sydney, Sydney, New South Wales, Australia

[5]Surgical & Orthopaedic Research Laboratories (SORL), Prince of Wales Clinical School, UNSW Sydney, Sydney, New South Wales, Australia

[6]Prince of Wales Hospital, School of Medicine, UNSW Sydney, Sydney, New South Wales, Australia

[7]School of Medical Sciences, The University of Sydney, Camperdown, New South Wales, Australia

[8]Mark Wainwright Analytical Centre, UNSW Sydney, Sydney, New South Wales, Australia

[9]Department of Mechanical and Industrial Engineering, University of Toronto, Toronto, Ontario, Canada

Correspondence
Florence H. Y. Lui and Charles C. Sorrell, School of Materials Science and Engineering, Hilmer Building, Gate 2 Avenue, UNSW Sydney, Sydney, NSW 2052, Australia.
Email: f.lui@unsw.edu.au; c.sorrell@unsw.edu.au

Abstract

A contiguous carbonate-rich hydroxyapatite microcoating in a microfluidic device represents a substrate that has chemical and structural similarity to bone mineral. The present work describes a low-temperature method to deposit a carbonate-rich hydroxyapatite microcoating on a glass slide and its incorporation within the microchannels of a microfluidic device. A glass slide is covered/masked with polypropylene-based tape and $CaCO_3$ nanoparticles are deposited on exposed areas by convective self assembly. The precursor $CaCO_3$ is converted to carbonate-rich hydroxyapatite by dissolution-recrystallization in phosphate-buffered saline. The microcoating is aligned/incorporated within a microchannel when the underlying glass is bonded to a polydimethylsiloxane structure with the device layout. X-ray diffraction, laser Raman microspectroscopy, and X-ray photoelectron spectroscopy indicate that the microcoating was comprised of carbonate-rich hydroxyapatite. Scanning electron microscopy and 3D laser confocal microscopy showed that was comprised of nanocrystalline rod-like clusters that collectively exhibit a thickness of ~20 μm. Monocultures/cocultures of osteoblast-lineage (MC3T3-E1, MG63) and preosteoclast-

lineage (RAW 264.7) cells were performed. Osteoblast-lineage cells adhered to the microcoating and deposited an extracellular matrix of collagen fibrils and mineral accretions. Mineralization was detected in/near the inlet wells. The microcoating is analogous to bone mineral and could be applied to various layouts and mineral systems.

KEYWORDS
bone-on-a-chip, carbonate hydroxyapatite, microfluidic, mineralization, osteoblast

1 | INTRODUCTION

Microfluidic devices that manipulate fluids in channels at the micron scale have been used widely to mimic the physiological environment and dynamic interactions within organs, such as lung,[1] kidney,[2] and intestine.[3] Key advantages of these *organ-on-a-chip* platforms include the ability to use human cells, replicate 3D physiological microenvironments, model cell–cell and cell-matrix interactions, and exert a high degree of control over parameters.[4]

Bone-on-a-chip platforms are a relatively recent development in the field, where studies focus primarily on channel/layout designs that replicate the physiological characteristics of bone and associated diseases.[4–7] In addition to a hierarchical structure[8] and the bone cells that orchestrate the bone remodeling process,[9] another key defining characteristic of bone is its matrix components: carbonate-rich hydroxyapatite (~70 wt%) and collagen (~30 wt%).[10] Conventional microfluidic devices comprise of a poly-dimethyl-siloxane (PDMS)-on-glass configuration that differs from bone in terms of chemical composition and crystallography.

Strategies to replicate bone minerals in microfluidic devices primarily involve the insertion of loose particles or scaffolds after polydimethylsiloxane (PDMS) is bonded to a glass slide (Figure 1). In 2012, Lee et al.[11] incorporated micropatterns that were loaded with antibiotics and biphasic calcium phosphate particles with the goal of high throughput screening of materials. In 2018, Sieber et al.[12] placed a hydroxyapatite-coated zirconium oxide scaffold into a microfluidic device. In 2019, Ahn et al.[13] mixed hydroxyapatite particles with fibrin to form an organic-mineral composite. Most recently in 2020, Bahmaee et al.[14] incorporated a polymerized high-internal-phase-emulsion scaffold into a microfluidic platform to facilitate osteogenesis. The scaffolds were not incorporated within the microchannels; the minerals were otherwise deposited by solution-based methods that could not target specific areas of the microchannels.

These studies also have focused exclusively on hydroxyapatite[11–13] There is opportunity to incorporate carbonate-rich hydroxyapatite in microfluidic devices because it has greater similarity to bone mineral in terms of chemical composition.[15,16] It also is bioresorbable by osteoclasts,[15] which may be advantageous for *bone-on-a-chip* platforms that aim to model osteoclast-mediated bone diseases such as osteoporosis, bone tumors, and Paget's disease.[17]

Incorporation of a contiguous carbonate-rich hydroxyapatite microcoating in microfluidic devices represents a research gap. It is hypothesized that a mineral microcoating could be deposited on select areas of a glass slide if other regions are masked/covered (e.g., by polypropylene-based tape) (Figure 1). Polypropylene-based tape is used in this study as a simple method to demonstrate that a pre-PDMS bonding process for incorporating a microcoating comprised of carbonate-rich hydroxyapatite in the microchannels of a microfluidic device is feasible; demonstrated strategies such as the use of computer aided design (CAD) or lithography techniques to form the mask/cover could be adopted for subsequent studies. The microcoating, which would have a fixed position on the glass slide, could then be aligned to fit within a microchannel of a microfluidic device when the underlying glass is bonded to a PDMS structure with the device layout. The key advantage of this approach is that the microcoating could be deposited selectively on a specific area of the glass slide that corresponds to target regions of microchannels; this is highly beneficial for microfluidic devices with complex layouts and designs intended to have multiple microenvironments.

A suitable low-temperature technique to deposit a carbonate-rich hydroxyapatite microcoating onto exposed areas of a glass slide has been described by Lui et al.[18,19] Briefly, $CaCO_3$ nanoparticles ($CaCO_3$-NP) can be deposited on the exposed area of a glass slide by convective self-assembly (CSA)[18] (Figure 1). The precursor $CaCO_3$ then can be converted to carbonate-rich hydroxyapatite by dissolution-recrystallization in a

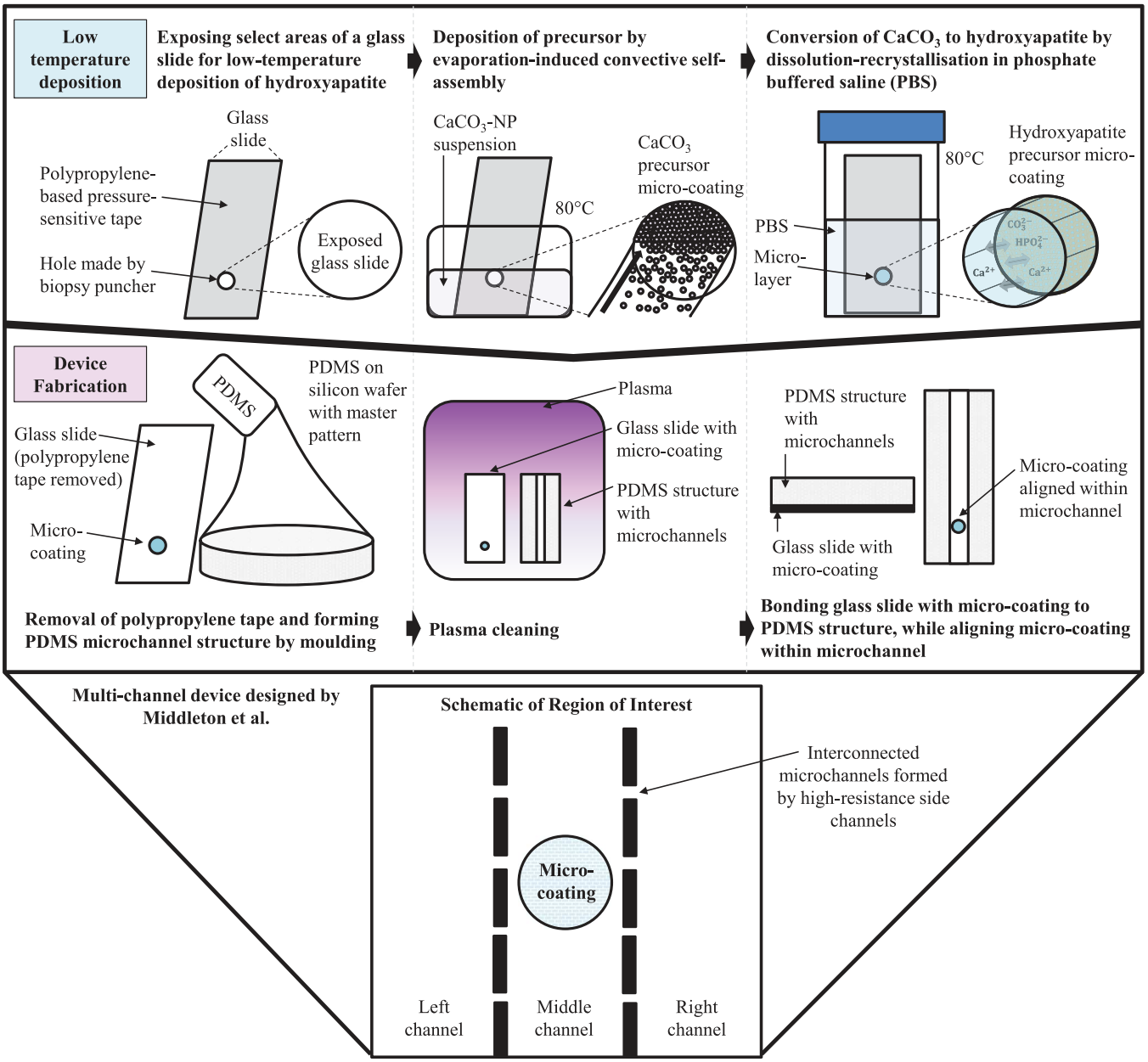

FIGURE 1 Schematic diagram of the low-temperature deposition method to form a microcoating of carbonate-rich hydroxyapatite and incorporate it within the microchannels of a microfluidic device. Low-temperature deposition: A glass slide is covered/masked with polypropylene-based tape and $CaCO_3$ nanoparticles ($CaCO_3$-NP) are deposited on exposed areas by convective .[18] The precursor $CaCO_3$ is converted to carbonate-rich hydroxyapatite by dissolution-recrystallization in phosphate-buffered saline (PBS).[19] Device fabrication: The tape is removed; in a separate process, PDMS is poured on a silicon wafer with the microfluidic design to form a mould of the device layout. The glass slide with the microcoating and the PDMS structure then are tplasma-treated and bonded; the microcoating is aligned within a microchannel during this process. Device design: The microfluidic device used in the present study was designed by Middleton et al.[7] and has multiple interconnected channels

phosphate-containing solution.[19] The microcoating then can be aligned/incorporated within a microchannel when the underlying glass is bonded to a polydimethylsiloxane structure with the device layout.

This technique is suitable for pre-PDMS bonding, rather than after the PDMS is bonded (which is typical of previous studies). Rationale for a pre-PDMS bonding process includes: The small volume of microchannel is not conducive to $CaCO_3$ dissolution, which underpins the dissolution-recrystallization process for conversion to carbonate-rich hydroxyapatite. Further, the shear stress created by fluid flow injection when the $CaCO_3$-NP suspension is replaced by PBS may dislodge the $CaCO_3$-NPs; adhesion strength of the microcoating is improved during

the dissolution-recrystallization process to carbonate-rich hydroxyapatite.

Materials characterization of the microcoating was performed in order to determine crystallographic, chemical, and morphological properties of the microcoating. X-ray diffraction (XRD), laser Raman microspectroscopy (Raman), Fourier-transform infrared spectroscopy (FTIR), and X-ray photoelectron spectroscopy (XPS) were performed to determine its phase composition. Scanning electron microscopy (SEM) and 3D confocal microscopy (3D microscopy) were performed to determine the morphology, thickness, and topographical roughness.

The principal originality of the present study lies in the incorporation of a carbonate-rich hydroxyapatite microcoating within the microchannels of a microfluidic device. In vitro characterization using osteoblast-lineage cells (MC3T3-E1, MG63) and preosteoclast-lineage cells (RAW 264.7) has been performed in order to assess suitability for *bone-on-a-chip* and *tissue-engineering-on-a-chip* applications. The tests have been designed to provide preliminary indicative information on mineralization, extracellular matrix, growth, and chemotaxis. In addition to imaging (optical, SEM), histological staining, such as Alizarin red staining to assess mineralization, and crystal violet staining for quantitative analysis of cell migration, have been performed.

2 | RESULTS AND DISCUSSION

2.1 | Materials characterization of the micro-coating

2.1.1 | Thickness

3D microscopy was performed to determine the thickness of the microcoating. The 3D confocal micrograph of the microcoating is shown in Figure 2A. The difference between maximal and minimal heights of the microcoating on glass was 19 ± 1.4 μm; this indicates that the microcoating would fit within the microchannel of the microfluidic device, which has a height of 60 μm.

The thickness of the microcoating is driven by the low-temperature deposition process, where a precursor $CaCO_3$-NP microcoating is deposited onto an exposed area of a glass slide by the CSA technique and subsequently converted to carbonate-rich hydroxyapatite through dissolution-recrystallization processes in PBS.[18]

The CSA technique induces the self-assembly of $CaCO_3$-NPs toward the triple contact line of liquid ($CaCO_3$-NP suspension), solid (glass), and vapor phase (air) due to capillary forces at the meniscus when the suspension evaporates.[24,25] The contact angle is a key determinant of deposition thickness[18,24,25] and previous studies that used a similar low-temperature deposition method to deposit a contiguous microfilm of carbonate-rich hydroxyapatite on polyether-ether-ketone (PEEK) reported a film thickness of <3 μm.[18] In addition to substrate type (PEEK vs. glass), other factors that may have contributed to the differences in thickness include temperature (130°C vs. 80°C), angle at which the sample was placed in the suspension, and the presence of the polypropylene-based tape that surrounds the exposed area of the glass slide.

The dissolution-recrystallization process that converts the $CaCO_3$ precursor to carbonate-rich hydroxyapatite also may influence the thickness of the resultant microcoating. Previous studies that used the same process (i.e., immersion in PBS at 80°C for 24 hours) to convert free-standing $CaCO_3$ microfilms to carbonate-rich hydroxyapatite reported an 8% increase in thickness.[19] The increase in thickness was attributed to the outward growth of hydroxyapatite sheets that replaced rhombohedral calcite crystals.

2.1.2 | Morphology

SEM was performed to assess the morphology of the microcoating and the results are shown in Figure 2B. The microcoating is comprised of clusters of randomly oriented rod-like nanoparticles. Mohandes et al. have reported nanocrystalline hydroxyapatite particles with comparable morphology[26] that were produced by the reaction between a calcium–ligand solution and an ammonium hydrogen phosphate solution.

Comparison with microfilms of previous studies that applied the same dissolution-recrystallization process to convert precursor $CaCO_3$ to carbonate-rich hydroxyapatite could elucidate the key drivers of the morphology observed. In a previous study, a precursor $CaCO_3$ microfilm was formed at the air-solution interface of supersaturated $Ca(HCO_3)_2$ heated at 40°C for 24 hours.[19] In a separate study, a precursor $CaCO_3$ layer was formed on PEEK by CSA followed by a cold-sintering technique, where the samples coated with an initial $CaCO_3$-NP layer were immersed in a supersaturated solution of $Ca(HCO_3)_2$ at 130°C for 10 minutes in order to induce rapid nucleation and precipitation of $CaCO_3$ across the surface.[18] Although the precursor $CaCO_3$ films from all three studies were immersed in 10 mM PBS and incubated at 80°C for 24 hours, the resultant morphologies differed, as discussed below.

The free-standing microfilm was comprised of rosette clusters of sheets in the size range of ~15–30 μm,[19] the carbonate-rich hydroxyapatite coating on PEEK was comprised of ~1 μm rosette clusters of platelets,[18] while

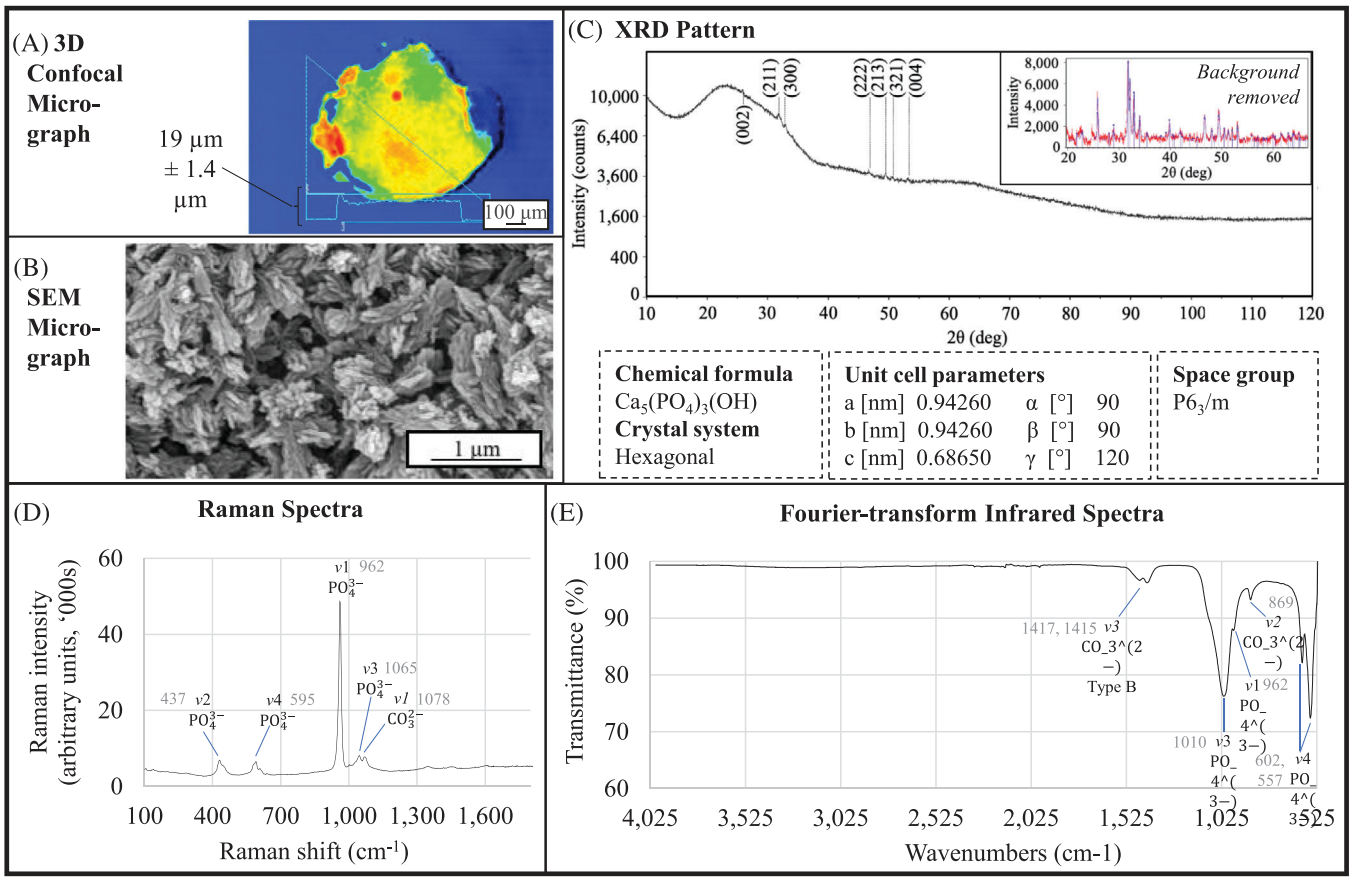

FIGURE 2 Materials characterization of the microcoating; (A) 3D laser confocal micrograph; (B) SEM micrograph; (C) XRD pattern (Top right: XRD pattern after subtraction of the amorphous glass background; reference used for phase identification: 04-007-2837); (D) Raman spectra; (E) Fourier-transform infrared spectra

the samples of the present study exhibit clusters of randomly oriented rod-like nanoparticles. Kumar et al.[27] have noted that the driving force for hydroxyapatite precipitation includes temperature and the supersaturation level of Ca^{2+} and PO_4^{3-} with respect to hydroxyapatite. All precursor $CaCO_3$ samples in these studies were subject to the same incubation temperature during the dissolution-recrystallization process. However, the size of the precursor $CaCO_3$ crystals differed. Smaller crystals exhibit larger surface areas, and these may cause higher rates of dissolution and supersaturation levels in the microenvironment.

The dissolution of $CaCO_3$ results in defects that become active sites for the nucleation carbonate-rich hydroxyapatite.[28] Preferential nucleation occurs over growth during the initial stages of the process, when the concentration of dissolved Ca^{2+} is higher. This is consistent with the morphologies observed for the free-standing microfilm, PEEK coating, and the present study. The high surface area of the precursor $CaCO_3$-NPs in the present study would be conducive to $CaCO_3$ dissolution and result in higher saturation. This may increase the rate of nucleation, as observed in the high number of rod-like nanoparticles. This is consistent with the observations of Zaremba et al.,[29] where precursor nanoparticles of $CaCO_3$ resulted in the reprecipitation of numerous nano-hydroxyapatite crystallites following dissolution-recrystallization in a phosphate solution.

2.1.3 | Crystallography

An XRD pattern of a microcoating on a glass slide is shown in Figure 2C. The intensities are low owing to the small volume of material (<1 mm^2) and the large hump is attributed to the amorphous glass substrate. Sharp peaks are readily visible after the amorphous hump was subtracted from the pattern (top right corner), indicating that the microcoating is well crystallized. No preferred orientation was detected. This is consistent with the SEM results, where the rod-like nanoparticles appear to be growing in random directions. Phase identification of the diffraction peaks confirms that the microcoating is comprised of hydroxyapatite.

2.1.4 | Chemical composition

Hexagonal hydroxyapatite and carbonate-rich hydroxyapatite are isostructural,[18] so laser Raman was performed in order to determine whether the microcoating contains carbonate peaks. The laser Raman spectra of the sample is shown in Figure 2D. A strong phosphate *v1* symmetric stretch for hydroxyapatite is observed, as well as the *v2*, *v3*, and *v4* phosphate peaks.[30] Additionally, the main carbonate *v1* symmetric stretch characteristic of carbonate-rich hydroxyapatite is present.[30] However, the main *v1* calcite peak at 1085 cm^{-1} is not observed.[31] This indicates that the microcoating is comprised of carbonate-rich hydroxyapatite.

FTIR was performed for further elucidation of the chemical composition of the sample. PO_4^{3-} ions can be substituted with CO_3^{2-} ions in carbonate-rich hydroxyapatite and FTIR is a very useful tool to detect carbonate in hydroxyapatite because it is sensitive to even a very small amount of carbonate.[32] Figure 2E shows the FTIR spectrum for the sample. Key phosphate peaks were observed, including the *v1*, *v3*, and *v4* phosphate peaks. The *v3* carbonate vibrations of C–O are in the high-energy region between 1410 and 1470 cm^{-1} and the *v2* carbonate vibrations are in the low-energy region between 850 and 890 cm^{-1}. The *v3* peaks are assigned to Type B carbonate-rich hydroxyapatite, where PO_4^{3-} ions are substituted by CO_3^{2-} ions rather than by OH^- ions, which is characteristic of Type A carbonate-rich hydroxyapatite.[33] The FTIR spectra did not contain any absorption bands from the substrate (i.e., glass slide), indicating that the entire surface was coated.

The Ca/P ratio is used commonly to identify calcium phosphates. Stoichiometric hydroxyapatite has a Ca/P ratio of 1.67, whereas carbonated calcium-deficient hydroxyapatite and bone minerals have a Ca/P ratio of ~1.5–1.6.[22,30,31] The XPS data showed that the Ca/P ratio of the microcoating was 1.7 ± 0.2, which is the average of three distinct samples (Ca/P ratios of 2.0, 1.6, and 1.5). The higher Ca/P ratio of 2.0 may be attributed to the substitution of PO_4^{3-} ions by CO_3^{2-}, which would lead to a higher Ca/P ratio due to a relative decrease in P. The microcoating is not tetracalcium phosphate (TTCP, $Ca_4P_2O_9$) despite it having a Ca/P ratio of 2.0; TTCP was not detected by XRD or Raman. Further, hydroxyapatite is less soluble than TTCP and would precipitate preferentially during the dissolution-recrystallization processes used to fabricate the samples.[37] Another possible explanation may be the presence of remnant $CaCO_3$; an inflated Ca/P ratio due to remnant calcite has been reported previously for mineral microfilms with a hybrid structure of $CaCO_3$ and carbonate-rich hydroxyapatite.[19] However, $CaCO_3$ was also not detected by XRD or Raman.

The materials characterization results indicate that the microcoating is comprised of nanocrystalline carbonate-rich hydroxyapatite. The use of $CaCO_3$-NPs as a precursor for conversion to carbonate-rich hydroxyapatite by immersion in PBS has been reported previously reported and the possible mechanism was described in detail.[18,19] This dissolution-recrystallization process also has been reported by Ratner et al.[29] and Mann et al.,[38] albeit at high temperatures under hydrothermal conditions. Briefly, hydroxyapatite has lower solubility than $CaCO_3$ and other calcium phosphates, so hydroxyapatite would precipitate preferentially as $CaCO_3$ dissolves, and the solution becomes saturated with respect to hydroxyapatite. This dissolution-recrystallization process occurs as long as sufficient $CaCO_3$ dissolves and the solution becomes saturated (i.e., conditions are conducive to $CaCO_3$ dissolution, and the volume of the solution is not too large). The system in the present study is designed to enable the conversion of the microcoating from $CaCO_3$ to hydroxyapatite.

2.2 | In vitro characterization

2.2.1 | Co-culture: in vitro characterization

Optical microscopy was performed daily for 14 days in order to monitor changes in the growth patterns of monocultures of osteoblast-lineage cells (MC3T3-E1, MG63). Optical micrographs at day 3 and day 14 are shown in Figure 3A and C. Both cell types were seeded in the left channel and show a similar growth pattern. The cells grew toward the middle channel as the left channel became increasingly confluent. Cells in devices with and without a microcoating grew in a similar way. The key difference was that cells around the microcoating grew around it and formed a concentric pattern, as shown in Figure 3Aiv and Civ.

Monocultures of preosteoclast-lineage cells (RAW 264.7) are shown in Figure 3B. The cells remain mononuclear throughout the 14-day period, as shown in Figure 3Bii and Biv. Figure 3B shows that the RAW 264.7 cells grew into the middle channel from the right channel in large clusters, probably as the left channel became increasingly confluent. Figure 3Biv shows that the RAW 264.7 cells grew in multiple layers. This was observed in devices that did and did not contain a microcoating.

Co-cultures of osteoblast-lineage (MC3T3-E1, MG63) and preosteoclast-lineage cells (RAW 264.7) are shown in Figure 3D and E. Osteoblast-lineage cells were seeded in the left channel and preosteoclast-lineage cells in the right channel. No notable differences were observed between devices with and without a microcoating. Cell growth in the coculture systems were similar to that observed in the

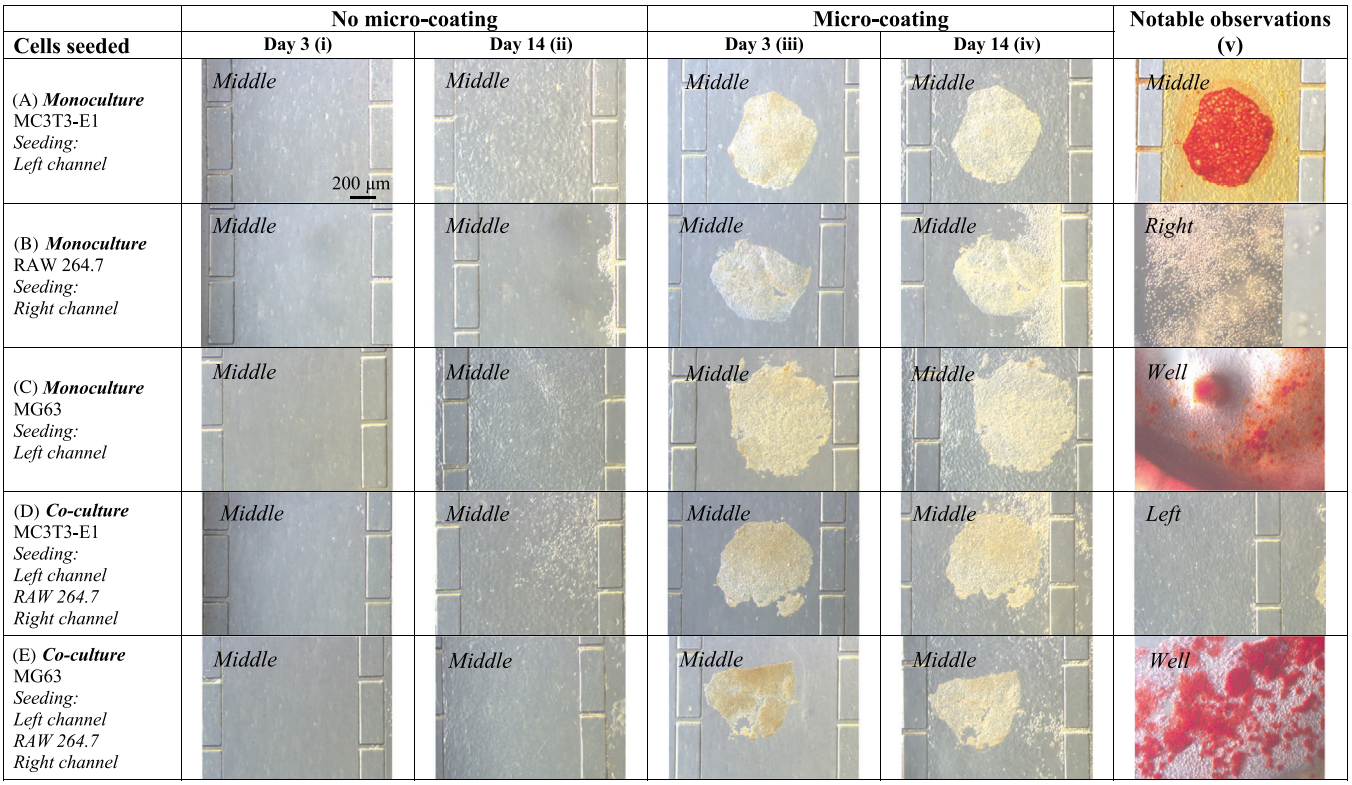

FIGURE 3 Monocultures and co-cultures for assessing growth patterns and mineralization; Monoculture MC3T3-E1: i-ii) No micro-coating – middle channel on day 3 and day 14; iii-iv) Micro-coating - middle channel on day 3 and day 14; v) Calcium staining on the micro-coating during treatment with Alizarin red; Monoculture RAW 264.7: i-ii) No micro-coating - middle channel on day 3 and day 14; iii-iv) Micro-coating - middle channel on day 3 and day 14; v) Monocytes remain mononuclear on day 14; Monoculture MG63: i-ii) No micro-coating - middle channel on day 3 and day 14; iii-iv) Micro-coating - middle channel on day 3 and day 14; v) Typical bright red Alizarin staining observed on a confluent cell mat, and mineralized nodule in the MG63 inlet well; Co-culture MC3T3-E1/RAW 264.7: i-ii) No micro-coating - middle channel of the on day 3 and day 14; iii-iv) Micro-coating - middle channel on day 3 and day 14; v) Confluent mat; Co-culture MG63/RAW 264.7: i-ii) No micro-coating – middle channel of the on day 3 and day 14; iii-iv) Micro-coating - middle channel on day 3 and day 14; v) Significant Alizarin red staining in the MG63 inlet well. *Same scale bar of 200 µm (see a)i) is used for all micrographs

monoculture systems, where the cells became confluent in the channels in which they were seeded in and progressively migrated toward the middle channel. Cell aggregates of MG63 cells were observed in one of the MG63-RAW 264.7 coculture samples; subsequent mineralization assay performed on the sample indicated that the cell aggregate was not a mineralized nodule. The cell aggregate represents anomalous growth. RAW 264.7 cells remained mononuclear throughout the 14-day period, indicating that any RANKL that may have been produced by the osteoblast-lineage cells did not induce osteoclastogenesis.

2.2.2 | Co-culture: Mineralization assay

The samples described in Section 2.2.1 were used to perform a mineralization assay by Alizarin red staining at day 14. The microcoating consistently stained bright red in all devices, indicating the presence of calcium. This is consistent with the materials characterization results shown in Section 2.1, which indicated that the microcoating is comprised of carbonate-rich hydroxyapatite. The Alizarin red stain on the microcoating during the early stages of the staining process is shown in Figure 3Av. A net-like pattern reminiscent of the ridges on the outer rind of a cantaloupe is observed. The unstained areas may indicate the location of cells, which represents an initial barrier layer between the underlying mineral and the Alizarin red stain. The entire planar view of the microcoating stains bright red by the end of the incubation period, either because the matrix vesicles and mineralized nodules on the cells eventually stained after a longer incubation period (Figure 3C,Ei) or the stain gradually diffused through the entire mineral structure (Figure S1a).

No bright red staining was observed in the interconnected channels of osteoblast-lineage monoculture and coculture samples, albeit the confluent cell sheets displayed a pink tinge (Figure 1b). Small, isolated patches of

bright stains were observed in the interconnected channels during the incubation period, but they lost their hue after rinsing (Figure 1c). These may be due to a small volume of mineralized nodules during the transition from primary to secondary bone mineralization. Bright red staining in the gaps between the high resistance channels was observed in a few devices, but this was attributed to trapped debris rather than in vitro mineralization (Figure S1d).

Conversely, Figure 3cv and Ev, and Figure S1e shows that the inlet wells of monocultures and cocultures of osteoblast-lineage cells (MC3T3-E1, MG63) displayed bright red staining typical of in vitro mineralization. The cell aggregate resembling a bone nodule in Figure 3Cv was observed in the MG63 inlet well of a monoculture sample. Mineralization also was observed in the microchannel near the inlet wells for osteoblast-lineage cells (Figure S1f). The in vitro mineralization observed in/near the inlet wells of osteoblast-lineage cells are attributed to a higher density of cells in the wells and access to nutrients. Future *bone-on-a-chip* tissue engineering studies could optimize the system fin terms of these parameters (higher seeding density and continuous flow) for accelerated mineralization and bone growth.

Figure 3Bv shows a monoculture of RAW 264.7 cells after Alizarin red staining. No bright red stains characteristic of in vitro mineralizationweres observed, albeit the cells exhibited a light pink tinge.

The coculture in vitro characterization and mineralization assay results suggest that seeding density and access to nutrients may have been the key limiting factors to mineralization throughout the microfluidic device; future studies targeting in situ mineralization or bone formation could use a higher seeding density, apply continuous flow, and optimize the cell culture medium used (e.g., differentiation media).

2.2.3 | Monoculture: Morphological characterization

Figure 4 shows the morphology of MC3T3-E1 and MG63 on/near the microcoating at various magnifications after 7 days of growth.

Figure 4A is a micrograph of the microcoating at low magnification; the light areas represent the microcoating, and the dark areas represent MC3T3-E1 cells growing on it. The cells are distributed across the microcoating relatively uniformly. Figure 4B is the corresponding micrograph for a MG63 sample, where the cells are more confluent. This indicates that MG63 grows and proliferates at a higher rate than MC3T3-E1, though the microcoating is biocompatible with both cell types.

Figure 4C shows MC3T3-E1 growing on the microcoating at higher magnification. The cells display the typical spreading behavior of adherent cells. Lamellipodium are attached on the microcoating and form gap junctions with adjacent cells. The corresponding micrograph for a MG63 sample is shown in Figure 4D. The cells exhibit similar spreading and adherent behavior to the MC3T3-E1 cells. These observations indicate that the microcoating promotes cell adhesion.

Additionally, nano-fibrils and small (10–15 μm) globules on the cells were observed in Figure 4D. Bone mineralization is comprised of a primary and secondary.[39] The primary phase is orchestrated mainly by osteoblasts, which secrete a large amount of type 1 collagen fibrils, noncollagenous proteins and growth factors, and extracellular matrix vesicles. This is followed by secondary mineralization, where there is an increase in bone mineral density driven by physiochemical crystal maturation. Matrix vesicles are encapsulated initially by a plasma membrane and calcium phosphate minerals eventually penetrate through the membrane to form mineralized nodules that interact with the extracellular environment for continued crystal nucleation and growth. The fibrils observed in Figure 4D may represent collagen fibrils secreted by the cells during the primary phase of bone mineralization. Previous studies have attributed similar globules to mineralized nodules or preosteoblastic-osteoblasts with collagen fibrils and matrix vesicles.[39–41]

Figure 4E shows a high magnification micrograph of a MC3T3-E1 cell on the microcoating. A dense network of fibrils and some accretions are observed on the surface of the cell. The fibrils are ~70 nm in width, consistent with type 1 collagen fibrils in the bone extracellular matrix during the early stages of bone development.[42,43] Similar morphological cell-matrix interactions in mineralizing cells are reported by Fernandes et al. 2009.[44] The corresponding micrograph for a MG63 sample is shown in Figure 4F. A dense layer of cells completely covers the microcoating. A haphazard arrangement of collagen fibrils is observed. Matrix vesicles are observed as aggregates in some areas or scattered among collagen fibrils in others, consistent with previous studies that show aggregates of matrix vesicles on mineralizing osteoblasts.[45–47] This further suggests that the cells are engaged in the primary phase of mineralization.

Figure 4G shows the cell-matrix interactions for MC3T3-E1 samples at high magnification. The corresponding micrograph for a MG63 sample is shown in Figure 4H. The high level of cell-matrix interaction on the mineral layer may contribute toward the reduction of cell proliferation[44] as higher confluence was observed in cells growing on the glass surrounding the mineral layer.

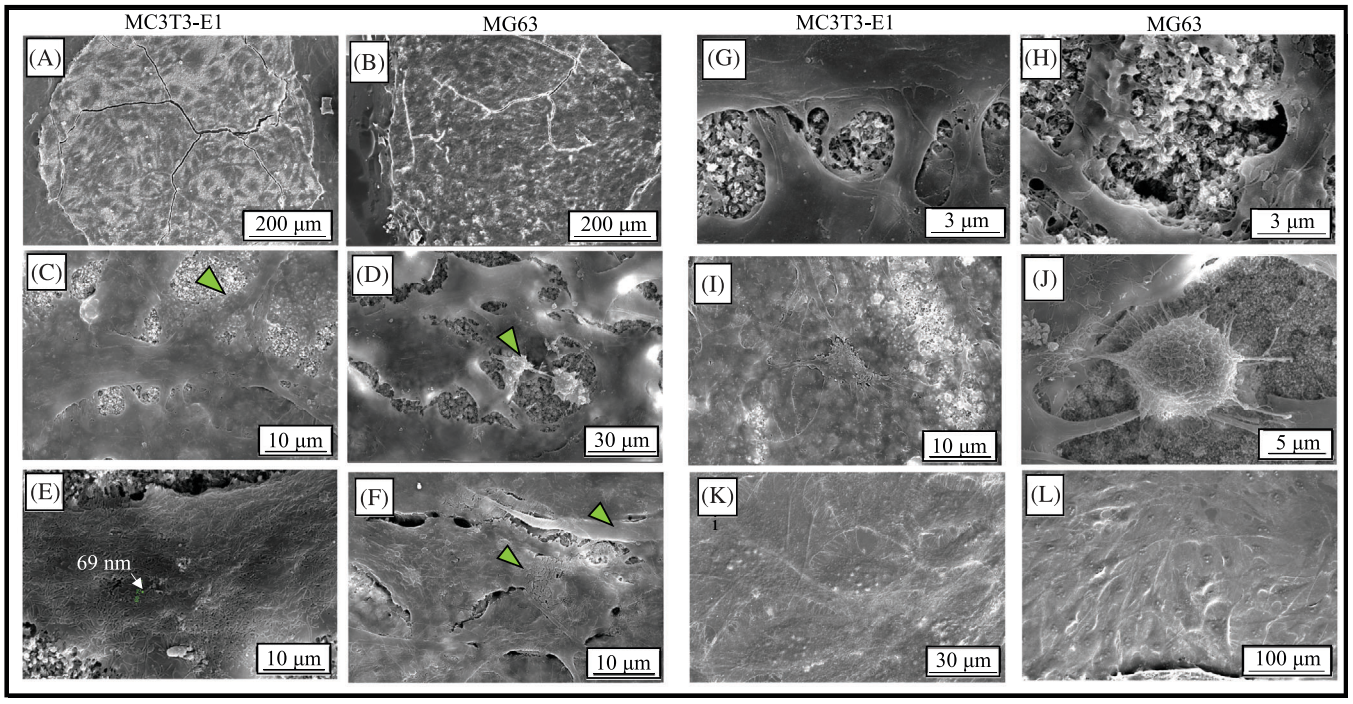

FIGURE 4 SEM micrographs of osteoblast-lineage cells on the microcoating and surrounding glass; (A) MC3T3-E1 on the micro-coating - dark regions represent cells, while light regions represent the microcoating – corresponding micrograph for a MG63 sample is shown in (B); (C) Higher magnification of MC3T3-E1 cells on the microcoating – cells exhibit typical spreading and adherent morphology, with multiple lamellipodia and gap junctions; (D) Higher magnification of MG63 growing on the microcoating – mineralized nodules are observed; (E) High magnification image of a MC3T3-E1 cell on the microcoating – accretions and a dense and haphazard network of fibrils (~70 nm in width) is observed on the surface of the cell; (F) Higher magnification of MG63 cells on the microcoating – the cells are confluent, and the microcoating is scarcely visible. Collagen fibrils and matrix vesicles are observed on the surface of the cells; (G) High magnification image of MC3T3-E1 cell-matrix interaction – corresponding micrograph for a MG63 samples is shown in (H); (I) A smaller cell (~10 µm) with anomalous morphology – it appears to be embedded in the underlying cells; (J) A smaller cell (~10 µm) with anomalous morphology is observed on the microcoating; (K) MC3T3-E1 on glass – cells are confluent and exhibit overlapping growth. The cells have a flattened morphology, and the cell nuclei are visible – corresponding micrograph for a MG63 sample is shown in L)

The cell highlighted in Figure 4I is ~5–10 µm. It has a flattened morphology and appears embedded in an underlying cell while exhibiting multiple filipodia, indicative of spreading and attachment. Franz–Odendaal et al. have noted that the transformation of osteoblasts to osteocytes is characterized by morphological changes such as a decrease in cell body size and the number of cell processes.[41] However, the rounded features on its surface also resemble membrane blebs, which may suggest that the cell is in the early stages of apoptosis.[48] Similarly, a cell with anomalous morphology also was observed in a MG63 sample and is shown in Figure 4J. The cell has a rounded morphology with filipodia spreading in all directions. There is a dense network of fibrils and rounded accretions on the cell's surface. Previous studies have reported a similar morphology for cells 1 hour after seeding;[49] cell migration may be a possible reason why the cell has retained this rounded morphology. It also bears some resemblance to the globules observed in Figure 4D. The observations in Figure 4I and J represent outliers as most cells on the microcoating spread to ~50–100 µm and exhibited the morphology shown in other micrographs.

Figure 4K shows MC3T3-E1 growing on glass near the microcoating. The cells exhibit the typical spreading and adhesion morphology. The cells exhibit a flattened morphology, and the cell nuclei are visible. The same observations are made for MG63 samples in Figure 4L. Some studies have attributed similar features to matrix vesicles emerging from the cell membrane.[50]

The results in Sections 2.2.1 and 2.2.2 indicate that there were limited mineralized nodules on the microdeposit. However, osteoblast-lineage cells on the mineral surface appeared to be engaged in the primary phase of bone mineralization, as evidenced by the extracellular matrix of collagen fibrils, matrix vesicles, mineral accretions, and mineralized nodules shown in Figure 4.

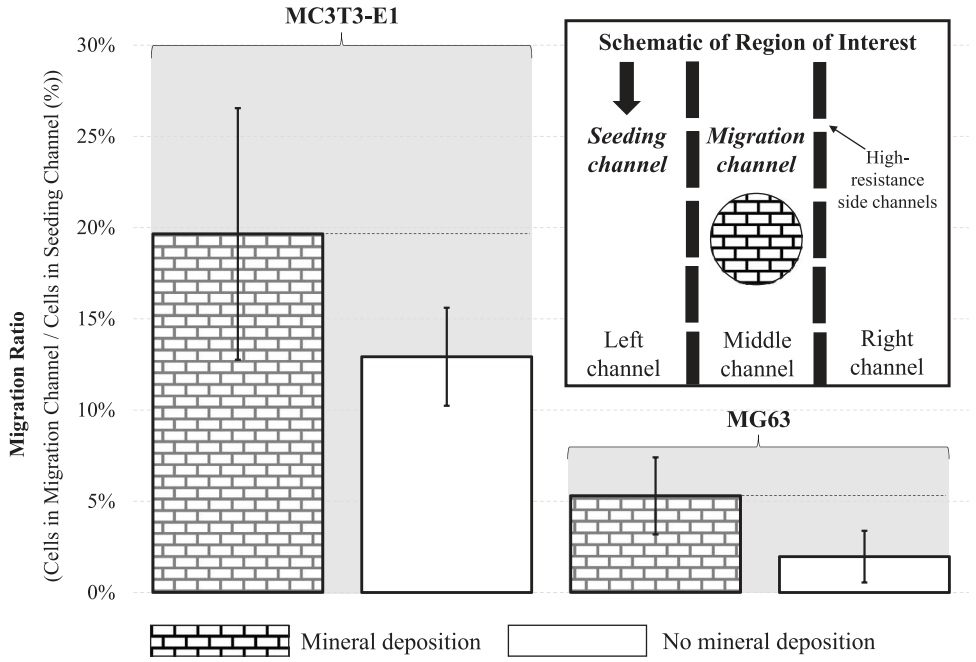

FIGURE 5 Chemotactic and proliferative effect of the microcoating on osteoblast-lineage cells; The schematic diagram shows the channel layout of the microfluidic device, where cells are seeded in the left channel and the microcoating is in the middle channel. The bar graph shows the Migration Ratio (ratio of the number of cells in the migration channel to the number of cells in the seeding channel) for MC3T3-E1 and MG63. Bars represent the mean of $n = 3$ replicates with SE. However, the mean Migration Ratio for samples with and without a microcoating was not statistically different ($p = 0.21$)

2.2.4 | Monoculture: Chemotaxis and proliferation assay

The chemo-attractive and proliferative effect of the microcoating on osteoblast-lineage cells (MC3T3-E1, MG63) was assessed. Figure 5 shows the microchannel layout of the microfluidic device used in the present work.[7] It consists of three parallel and interconnected cell culture channels. Each channel is separated by high-resistance side channels that minimize convection between the microchannels, thus limiting barrier-less cell growth and diffusion of cell culture media. A monoculture of osteoblast-lineage cells was selected to minimize the effects of crosstalk between different cell types and the mixing of different cell culture medium. The microcoating is in the middle channel (migration channel) and cells were seeded in the left channel (seeding channel) at a density of 4×10^5.

The Migration Ratio was selected to account for slight differences in seeding density, which may have a compound effect on the final cell count because the experiment ran for 7 days; 7 days was determined to be the optimal time point for monitoring cell migration from the seeding channel to the migration channel – there was minimal migration for shorter durations and proliferation/growth may dominate with longer durations.

The bar graph in Figure 5 shows the Migration Ratio for devices with and without a microcoating. The microcoating was associated with a 20% ± 7% (SE) Migration Ratio for MC3T3-E1 samples, whereas the corresponding value for devices with no microcoating was 13% ± 3% (SE). The microcoating was associated with a 5% ± 2% (SE) Migration Ratio for MG6 samples, whereas the corresponding value for samples with no microcoating was 2% ± 1% (SE).

There was no statistical difference in the mean Migration Ratio between samples with and without a microcoating ($p = 0.21$, $n = 3$), possibly due to the small sample size as a higher mean Migration Ratio was observed for samples with a microcoating. Previous studies have demonstrated that high levels of calcium ions in a microenvironment have a chemo-attractive effect on MC3T3-E1 and induces DNA synthesis.[51,52] The chemical gradient formed may have stimulated the migration and proliferation of osteoblast-lineage cells, which are reported to express the calcium sensing receptor protein (CaR) that enables the sensing of extracellular levels of calcium ions.[53,54] Calcium also has been proposed as a coupling factor in the bone remodeling process, where the recruitment and maturation of osteoblast-lineage cells at the bone resorption site follows the release of calcium into the microenvironment when osteoclasts resorb bone.[55] This discussion focuses on calcium ions because the microcoating is comprised of carbonate-rich hydroxyapatite, and the release of calcium is considered the key chemoattractant in this system.

3 | CONCLUDING REMARKS

The present study has demonstrated that a contiguous mineral microcoating can be incorporated in a microfluidic device. Materials characterization demonstrated that the microcoating was comprised of nanocrystalline carbonate-rich hydroxyapatite. It could be applied to *bone-on-a-chip* microfluidic platforms used to study bone biology and skeletal diseases so that the substrate on which the cells grow is a mineral layer that resembles bone minerals rather than glass. The microcoating could also be used as a substrate for the in situ deposition of bone matrix proteins during the dissolution-recrystallization process in order to increase its similarity to bone.

In vitro characterization using osteoblast-lineage cells (MC3T3-E1, MG63) and preosteoclast-lineage cells (RAW 264.7) was performed. A combination of imaging (SEM and optical) and staining (Alizarin red and crystal violet) techniques were used to assess mineralization, extracellular matrix, growth, and chemotaxis. The results provided preliminary indication of suitability for incorporation in a *bone-on-a-chip* and *tissue-engineering-on-a-chip*. The originality of the present research is the incorporation of a carbonate-rich hydroxyapatite microcoating within the microchannels of a microfluidic device. Potential follow-on work, including *bone-on-a-chip* and *tissue-engineering-on-a-chip* studies, should provide more rigorous *in vitro characterization* methods (e.g., immunostaining or gene expression) for elucidation of cell behavior.

The described method is distinguished from previous studies that incorporated a hydroxyapatite scaffold or particles in a microfluidic device[1–4] in that it enables a contiguous mineral microcoating to be deposited in specific areas of a device; note that there have been published accounts of printed micropatterns formed by printing/lithography techniques on prefunctionalized glass substrates pre-PDMS bonding,[5] though these micropatterns were not of a mineral phase and comprised of hydroxyapatite or carbonate-rich hydroxyapatite. The area of the microcoating reported in the present work is relatively small. There is opportunity to build on the present work by forming microcoatings that correspond to larger areas of a microchannel and different device layouts. Specific mineral phases and thicknesses of the microcoating could be achieved by altering CSA parameters and reagents in the dissolution-recrystallization conversion process.

Finally, *medical-devices-on-a-chip*[56] are in the nascent stages of development; the microcoating is analogous to orthopedic implant coatings and could be applied to establish an *implant-on-a-chip* microfluidic model. This study has shown that it is possible to use CSA to deposit an initial layer of nanoparticles on glass for subsequent conversion to another phase through wet-chemical techniques. This suggests that the method could be applied to form a wide range of materials that may be representative of other biomaterials.

4 | MATERIALS AND METHODS

Preparation of $CaCO_3$ nanoparticulate suspension

Precipitated $CaCO_3$ nanoparticles ($CaCO_3$-NPs) (PlasmaChem GmbH; Berlin, Germany) were used as the raw materials to prepare $CaCO_3$ nanoparticulate suspensions ($CaCO_3$ suspensions, 0.1875 wt%) for coating deposition. $CaCO_3$-NPs were calcite, with average particle size of ~90 ± 15 nm. Ultrasonication was used to minimize agglomeration of the nanoparticles.

Preparation of poly–dimethyl–siloxane structures

A microfluidic device designed by Middleton et al.,[7] which consists of three parallel and interconnected cell culture channels (Width: 1 mm, Height: 60 μm), was used in the present work. Each channel is separated by high-resistance side channels (Length: 200 μm, Width: 20 μm, Height: 60 μm, Diffusion Gap: 20 μm) to minimize convection between channels. Poly-dimethyl-siloxane (PDMS) polymer and Sylgard® 184 curing agent (Sigma-Aldrich Pty Ltd, USA) were mixed at a ratio of 10:1 (by weight), poured onto a silicon wafer with the abovementioned device design, degassed in a vacuum chamber, and cured in an oven at 60°C. Once cured, inlet and outlet ports of the PDMS devices were bored using disposable 5 mm ⌀ biopsy punches (ProSciTech Pty Ltd; Australia).

Deposition of carbonate–rich hydroxyapatite

A biopsy puncher (ProSciTech Pty Ltd; Australia) with a 0.75 mm ⌀ cutting tip was used to form a hole on a sheet of polypropylene-based pressure-sensitive tape (Sellotape®; UK). The tape was adhered onto a glass slide with the hole positioned at the appropriate position. Additional sheets of tape were adhered to achieve full coverage of the glass slide to seal it from subsequent wet chemistry processes. The hole with exposed glass was cleaned with ethanol before further processing and then the glass slide was placed in a 20 ml beaker. A $CaCO_3$ suspension (20 ml) was poured into the beaker and placed into an oven preheated to 80°C. The glass slide was removed from the beaker after

the exposed glass was coated with a layer of $CaCO_3$-NP, which was formed by an evaporation-induced convective self-assembly technique.[18] A temperature lower than reported in previous studies was used to prevent thermal deformation/degradation of Sellotape® tape. The samples were air-dried and then incubated in a solution (15 ml) of phosphate-buffered saline (PBS, 10 mM, pH 7.6) at 80°C for 24 hours to convert the $CaCO_3$-NP layer to carbonate-rich hydroxyapatite.[18,19] The Sellotape® tape was removed and the samples were sequentially rinsed with deionized water and ethanol before further processing.

Device fabrication

The PDMS structures and coated glass slides were rinsed with isopropanol and bonded by oxygen plasma etching (2 minutes, ~45W, ~0.5 Torr) using a plasma asher (Plasma, etc./Asher PE-250; Denton Vacuum Inc., Moorestown, NJ, USA). The PDMS structures and coated glass slides were oriented for alignment with the microcoating in the middle channel. They were placed on a hot plate at 90°C for 10 minutes to facilitate initial bonding and then transferred to an oven preheated at 60°C. The devices were sterilized by 70% ethanol and followed by UV irradiation for 20 minutes before in vitro characterization.

Cell culture

Murine osteoblast-like cell line (MC3T3-E1), human osteosarcoma cell line (MG63), and murine macrophage cells (RAW 264.7) were used in the present study. MC3T3-E1 was cultured in Alpha-MEM (Gibco, Thermo Fisher Scientific, MA, USA) supplemented with 10% fetal bovine serum (FBS, Gibco FBS Qualified Australia Origin; Thermo Fisher Scientific, Waltham, MA USA), 1% penicillin/streptomycin (P/S, Sigma-Aldrich Pty. Ltd., MO, USA), and 1% L-glutamine (Sigma-Aldrich Pty. Ltd., MO, USA). MG63 and RAW 264.7 were cultured in Dulbecco's MEM (Gibco, Thermo Fisher Scientific, MA, USA) supplemented with 10% FBS, (Gibco FBS Qualified Australia Origin; Thermo Fisher Scientific, MA USA), 1% P/S (Sigma-Aldrich Pty. Ltd., MO, USA), and 1% L-glutamine (Sigma-Aldrich Pty. Ltd., MO, USA). The cell lines were incubated in a humidified atmosphere of 5% CO_2 at 37°C. MC3T3-E1 and MG63 were detached by trypsinization and RAW 264.7 cells were detached by a cell scraper. Detached cells were suspended in fresh culture media and used for further experiments as described below.

The in vitro characterization of the microcoating was performed using monocultures and cocultures of osteoblast-lineage and preosteoclast-lineage cells. The two osteoblastic cell lines used in this study were MG63 and MC3T3-E1. MG63 is a human osteosarcoma cell line commonly used as a stable in vitro characterization model of human osteoblast behavior and MC3T3-E1 is a similar murine cell line. MG63 was used in the study because it is a common cell line used for orthopedic studies and has greater relevance to *medical-devices-on-a-chip*, while the MC3T3-E1 is a standard cell line for *bone-on-a-chip* studies. Two osteoblast cell lines were used to enhance the relevance of the results to researchers in the in vitro bone research and orthopedics field. Static flow was used to retain the potential chemical gradient formed by the release of calcium ions from the microcoating.

The RAW 264.7 cell line is a virally transformed murine monocyte line that can be differentiated into macrophages following exposure to macrophage colony stimulating factor (mCSF) or osteoclasts following exposure to mCSF and osteoblast-secreted receptor activator of nuclear factor kappa B ligand (RANKL). The effect of the microcoating on the general growth patterns of osteoblast-lineage (MC3T3-E1, MG63) and preosteoclast-lineage (RAW 264.7) cells were assessed in monocultures and cocultures. Both osteoblast cell lines used are known to secrete mCSF and RANKL.[20–23]

Co-culture in vitro characterization

The sterilized devices were flushed with cell culture medium and cells were seeded passively into the channels at a density of 4×10^5; MC3T3-E1/MG63 were seeded into the left channel, RAW 264.7 was seeded into the right channel, and no cells were seeded in the middle channel with the microcoating (Table 1); devices without microcoatings were used as negative controls. For coculture devices, osteoblast lineage cells were seeded first and RAW 264.7 cells were seeded on the following day. The cells were cultured in the devices for 14 days and the cell culture medium was refreshed daily. Optical microscopy was performed daily for 14 days in order to monitor changes in their growth patterns and subsequently used for the mineralization assay; a time point of 14 days was selected for consistency with in vitro mineralization assays. A 50:50 media ratio of alpha MEM and DMEM was loaded in the middle channel of the MC3T3-E1/RAW 264.7 coculture device; 0.57 g L^{-1} of sodium hydrogen phosphate (Na_2HPO_4; Chem-Supply Pty. Ltd, Australia) and 0.006 g L^{-1} of sodium dihydrogen phosphate (NaH_2PO_4; Chem-Supply Pty. Ltd, Australia) were added to the medium used for the experiment. In situ optical microscopy was performed daily using an inverted optical microscope (Leica DM IL LED; Leica Microsystems GmbH, Germany/Jenoptik ProgRes CF_{scan} camera; Jenoptik

TABLE 1 Summary of samples

	RAW 264.7 *Passage 16*	MC3T3-E1 *Passage 7*	MG63 *Passage 118*	Co-culture in vitro characterization & mineralization assay [$n = 3$, 14 days]	Morphological characterization [$n = 2$, 7 days]	Monoculture chemotaxis assay [$n = 3$, 7 days]
No microcoating	Yes			✓		
		Yes		✓		✓
	Yes	Yes		✓		
			Yes	✓		✓
	Yes		Yes	✓		
Microcoating	Yes			✓		
		Yes		✓	✓	✓
	Yes	Yes		✓		
			Yes	✓	✓	✓
	Yes		Yes	✓		

Group, Germany) to assess cell morphology, growth, and migration.

Co-culture mineralization assay

Alizarin red staining was performed on the coculture in vitro characterization samples on day 14 to assess mineralization in the devices (Table 1). The channels of the microfluidic device were rinsed with 1X PBS, fixed with 4% paraformaldehyde (Electron Microscopy Sciences, USA), and rinsed again with 1X PBS. A 40 mM Alizarin red staining solution was applied to the microchannels and incubated at room temperature for 10 minutes and then rinsed with deionized water. Optical microscopy (Leica DM IL LED; Leica Microsystems GmbH, Germany/Jenoptik ProgRes CF_{scan} camera; Jenoptik Group, Germany) was performed to detect mineralization, which was indicated by areas that were stained bright red. A 40 mM Alizarin red staining solution was prepared by mixing 1 g of Alizarin red with 80 ml of deionized water and adjusting the pH to 4.1–4.3 by the addition of hydrochloric acid or ammonium hydroxide.

Morphological characterization of a monoculture

Samples (Table 1) were prepared for characterization by field emission scanning electron microscopy (FESEM, secondary electron mode at 15 kV) to assess the morphology of cells on the microcoating and surrounding glass after in vitro cell culture for 7 days. A 7-day time point was selected in order to enable growth before the cell mat becomes confluent, so that cell-matrix interactions on the microcoating still may be observed. The sterilized devices were flushed with cell culture medium and cells were seeded passively into the middle channel with the deposition at a density of 4×10^5. The samples were fixed with glutaraldehyde (Electron Microscopy Sciences, USA) in 0.1 M sodium cacodylate buffer at a final concentration of 2.5% for ~30 minutes, rinsed with 1X PBS, and dehydrated with ethanol (according to the series 30%, 50%, 70%, 80%, 90%, to 100% for 30 minutes each) and hexamethyldisilazane (HDMS, Reagent> grade > 99%; Sigma-Aldrich Pty Ltd, USA) according to the series 1:2 solution of HDMS : 100% ethanol, 2:1 HDMS : 100% ethanol, and 100% HDMS for 20 minutes each and air-dried for 48 hours. The samples then were adhered onto an aluminum SEM stub with carbon and copper tape. Platinum coating (Emitech K575x Pt sputter coater; Quorum Technologies Ltd., UK) was applied to further enhance the electrical conductivity of the samples.

Monoculture chemotaxis and proliferation assay

The sterilized devices were flushed with cell culture media and cells were seeded passively into the left channel at a density of 4×10^5 (Table 1); no cells were seeded in the middle channel with the microcoating; devices without microcoatings were used as negative controls. The cells were cultured in the devices for 7 days and the cell culture media was refreshed daily. On day 7, the cells were rinsed with 1X PBS, fixed with 4% paraformaldehyde (Electron Microscopy Sciences, USA), and rinsed again with 1X PBS. The fixed cells were stained with 0.5% crystal violet (Thermo Fisher Scientific, USA) for 10 minutes and rinsed with deionized water. Cells in the seeding channel (left

channel) and migration channel (middle channel) were imaged using an inverted optical microscope (Leica DM IL LED; Leica Microsystems GmbH, Germany/Jenoptik ProgRes CF_{scan} camera; Jenoptik Group, Germany) and counted. The Migration Ratio was used to determine the effect of the microcoating on cell chemotaxis and proliferation; the standard error (SE) values are reported ($n = 3$). Analysis of variance (ANOVA) was used to determine the statistical significance of the results.

4.1 | Materials characterization

X-ray diffraction (XRD, Smartlab; Rigaku Corporation, Japan; X-ray source Cu Kα, accelerating voltage 45 kV, current 200 mA, scan axis theta/2-theta, scanning range 10° to 120°, and scanning speed 8.4°/min for 50 hours) was used to determine the phase composition of the microcoating before in vitro characterization. Phase identification was performed using X'Pert HighScore Plus software (Malvern PANalytical; Malvern, UK).

Laser Raman microspectroscopy (Raman) (inVia 2, Renishaw plc, UK) was used to determine the phase composition of the microcoating before in vitro characterization. A green diode laser (532 nm) was used as the light source and key parameters include resolution (1.5 to 1.7 cm^{-1}), spot size (~1 μm), grating (1800 grooves mm^{-1}), and magnification (1000 X).

Fourier transform infrared spectroscopy (FTIR) (Bruker Vertex V80V Vacuum FTIR System, Bruker Corporation, USA) was used to identify surface functional groups and ions. Key parameters include spectral range: 4025 to 525 cm^{-1}, accumulations: 64, resolution: 4 cm^{-1}. Attenuated Total Reflectance (ATR) objective was used to increase the sensitivity of the analysis. An FTIR spectrum could not be obtained for a ~0.75 mm ⌀ microcoating (exposed area on the glass slide created by the biopsy puncher). Hence, a sample with a glass slide containing a 5 mm^2 exposed area was made for the FTIR analysis; all other fabrication steps were identical.

X-ray photoelectron spectroscopy (XPS) (ESCALAB 250Xi, ThermoFisher Scientific, USA) was used to determine surface calcium-to-phosphorus (Ca/P) ratio of the microcoating. Key parameters include X-ray source: Al K alpha, power: 160 W (14.5 kV × 11 mA).

Field Electron Scanning Electron Microscopy (FESEM, Nova NanoSEM 450 FESEM; FEI, USA; secondary electron mode at 15 kV) was used to assess the morphology of the microcoating before in vitro characterization. Carbon tape, copper tape, and platinum coating (Emitech K575x Pt sputter coater; Emitech Groupe, Montigny-le-Bretonneux, France) were used to enhance the electrical conductivity of the samples.

3D laser confocal microscopy (3D Microscopy, VK-X200; Keyence Corporation, Japan) was used to determine the thickness (defined as the difference between maximal and minimal height) of the microcoating before in vitro characterization ($n = 3$, 10X objective lens).

ACKNOWLEDGMENTS

The authors thank Dr. G. Yang (School of Materials Science and Engineering, UNSW Sydney), Dr. C.Y. Lin (Institute of Biomedical Engineering, University of Toronto), and U. Schubert (NSW Node of the Australian National Fabrication Facility) for assistance with characterization techniques, equipment set-up, and training. The authors thank Prof. M. D. Willcox, Dr. A. Vijay, and Dr. P. Kalaiselvan (School of Optometry and Vision Science, UNSW Sydney) for access to raw materials. The authors thank Dr. S. Yin (Mark Wainwright Analytical Centre, UNSW Sydney) for performing XPS. The authors thank Prof. L.A. Estroff (Department of Materials Science & Engineering, Cornell University) for access to facilities. This work was performed in part at the NSW Node of the Australian National Fabrication Facility. The authors acknowledge the facilities and the scientific and technical assistance of Microscopy Australia at the Electron Microscope Unit (EMU), the Cell Culture Facility within the Mark Wainwright Analytical Centre (MWAC) at UNSW Sydney, and the Cornell Centre for Material Research Shared Facilities (CCMR), supported by the NSF MRSEC program (DMR-1719875). The authors gratefully acknowledge financial support from the Australian Commonwealth Government via the Research Training Program and the Fulbright Futures Postgraduate Program, which is administered by the Australian Fulbright Commission and funded by the Kinghorn Foundation.

CONFLICT OF INTEREST

The authors declare no commercial or financial conflict of interest.

AUTHOR CONTRIBUTIONS

Conceptualization: Florence H. Y. Lui, Charles C. Sorrell, Lidan You, Pierrette Michaux; Methodology: Florence H. Y. Lui, Charles C. Sorrell, Lidan You, Liangcheng Xu, Pierrette Michaux, Yu Wang, Tara C. Brennan-Speranza, Joanna Biazik, Gregory F. S. Harm; Formal Analysis: Florence H. Y. Lui, Charles C. Sorrell, Lidan You, Yu Wang, Tara C. Brennan-Speranza, Joanna Biazik, Gregory F. S. Harm, Pramod Koshy; Writing – original draft: Florence H. Y. Lui; Writing – review and editing: all authors; Supervision: Charles C. Sorrell, Lidan You, Tara C. Brennan-Speranza, Pramod Koshy; Funding acquisition and resources: Charles C. Sorrell, Lidan You, Tara

C. Brennan-Speranza, Pramod Koshy, William R. Walsh, Ralph J. Mobbs, Rema A. Oliver.

DATA AVAILABILITY STATEMENT

The data that support the findings of this study are available from the corresponding author upon reasonable request.

REFERENCES

1. J. Shrestha, S. Razavi Bazaz, H. Aboulkheyr Es, D. Yaghobian Azari, B. Thierry, M. Ebrahimi Warkiani, M. Ghadiri, *Crit. Rev. Biotechnol.* **2020**, *40*, 213. https://doi.org/10.1080/07388551.2019.1710458
2. S. Musah, A. Mammoto, T. C. Ferrante, S. S. F. Jeanty, M. Hirano-Kobayashi, T. Mammoto, K. Roberts, S. Chung, R. Novak, M. Ingram, T. Fatanat-Didar, S. Koshy, J. C. Weaver, G. M. Church, D. E. Ingber, *Nat. Biomed. Eng.* **2017**, *1*. https://doi.org/10.1038/s41551-017-0069
3. S. Jalili-Firoozinezhad, F. S. Gazzaniga, E. L. Calamari, D. M. Camacho, C. W. Fadel, A. Bein, B. Swenor, B. Nestor, M. J. Cronce, A. Tovaglieri, O. Levy, K. E. Gregory, D. T. Breault, J. M. S. Cabral, D. L. Kasper, R. Novak, D. E. Ingber, *Nat. Biomed. Eng.* **2019**, *3*, 520. https://doi.org/10.1038/s41551-019-0397-0
4. A. Mansoorifar, R. Gordon, R. C. Bergan, L. E. Bertassoni, *Adv. Funct. Mater.* **2021**, *31*, 2006796. https://doi.org/10.1002/adfm.202006796
5. X. Mei, K. Middleton, D. Shim, Q. Wan, L. Xu, Y. H. V. Ma, D. Devadas, N. Walji, L. Wang, E. W. K. Young, L. You, *Integr. Biol.* **2019**, *11*, 119. https://doi.org/10.1093/intbio/zyz008
6. L. Xu, X. Song, G. Carroll, L. You, *Integr. Biol.* **2020**, *12*, 303. https://doi.org/10.1093/intbio/zyaa025
7. K. Middleton, S. Al-Dujaili, X. Mei, A. Günther, L. You, *J. Biomech.* **2017**, *59*, 35. https://doi.org/10.1016/j.jbiomech.2017.05.012
8. N. Reznikov, R. Shahar, S. Weiner, *Acta Biomater.* **2014**, *10*, 3815. https://doi.org/10.1016/j.actbio.2014.05.024
9. J. C. Crockett, M. J. Rogers, F. P. Coxon, L. J. Hocking, M. H. Helfrich, *J. Cell Sci.* **2011**, *124*, 991. https://doi.org/10.1242/jcs.063032
10. S. Von Euw, Y. Wang, G. Laurent, C. Drouet, F. Babonneau, N. Nassif, T. Azaïs, *Sci. Rep.* **2019**, *9*, 1. https://doi.org/10.1038/s41598-019-44620-6
11. J. H. Lee, Y. Gu, H. Wang, W. Y. Lee, *Biomaterials* **2012**, *33*, 999. https://doi.org/10.1016/j.biomaterials.2011.10.036
12. S. Sieber, L. Wirth, N. Cavak, M. Koenigsmark, U. Marx, R. Lauster, M. Rosowski, *J. Tissue Eng. Regener. Med.* **2018**, *12*, 479. https://doi.org/10.1002/term.2507
13. J. Ahn, J. Lim, N. Jusoh, J. Lee, T. E. Park, Y. T. Kim, J. Kim, N. L. Jeon, *Front. Bioeng. Biotechnol.* **2019**, *7*, 1. https://doi.org/10.3389/fbioe.2019.00168
14. H. Bahmaee, R. Owen, L. Boyle, C. M. Perrault, A. A. Garcia-Granada, G. C. Reilly, F. Claeyssens, *Front. Bioeng. Biotechnol.* **2020**, *8*, 1. https://doi.org/10.3389/fbioe.2020.557111
15. K. Ishikawa, *J. Ceram. Soc. Jpn.* **2019**, *127*, 595. https://doi.org/10.2109/jcersj2.19042
16. C. Rey, C. Combes, C. Drouet, M. J. Glimcher, *Osteoporos. Int.* **2009**, *20*, 1013. https://doi.org/10.1007/s00198-009-0860-y
17. H. Bi, X. Chen, S. Gao, X. Yu, J. Xiao, B. Zhang, X. Liu, M. Dai, *Front. Med.* **2017**, *4*, 1. https://doi.org/10.3389/fmed.2017.00234
18. F. H. Y. Lui, R. J. Mobbs, Y. Wang, P. Koshy, F. P. Lucien, D. Zhou, C. C. Sorrell, *Adv. Mater. Interfaces.* **2021**, *15*, 1. https://doi.org/10.1002/admi.202100333
19. F. H. Y. Lui, Y. Wang, Y. Yao, R. J. Mobbs, R. E. Pogson, P. Koshy, P. Frank, D. Zhou, C. C. Sorrell, *J. Colloid Interface Sci.* **2021**, *604*, 327.
20. M. S. Rybchyn, T. C. Brennan-speranza, D. Mor, Z. Cheng, W. Chang, A. D. Conigrave, R. S. Mason, *Int. J. Mol. Sci*, **2021**, *22*, 1. https://doi.org/10.3390/ijms22126509
21. R. A. Taichman, S. G. Emerson, *Exp. Hematol.* **1996**, *24*, 509.
22. T. Takaishi, T. Matsui, T. Tsukamoto, M. Ito, T. Taniguchi, M. Fukase, K. Chihara, *Am. J. Physiol. Cell Physiol.* **1994**, *267*, C25. https://doi.org/10.1152/ajpcell.1994.267.1.c25
23. M. Lamghari, L. Tavares, N. Camboa, M. A. Barbosa, *J. Cell. Biochem.* **2006**, *98*, 1123. https://doi.org/10.1002/jcb.20853
24. J. D. Joannopoulos, *Nature* **2001**, *414*, 257. https://doi.org/10.1038/35104718
25. C. N. Kaplan, N. Wu, S. Mandre, J. Aizenberg, L. Mahadevan, *Phys. Fluids* **2015**, *27*, 092105. https://doi.org/10.1063/1.4930283
26. F. Mohandes, M. Salavati-Niasari, M. Fathi, Z. Fereshteh, *Mater. Sci. Eng. C* **2014**, *45*, 29. https://doi.org/10.1016/j.msec.2014.08.058
27. R. Kumar, K. H. Prakash, P. Cheang, K. A. Khor, *Langmuir* **2004**, *20*, 5196. https://doi.org/10.1021/la049304f
28. P. Opitz, L. Besch, M. Panthöfer, A. Kabelitz, R. E. Unger, F. Emmerling, M. Mondeshki, W. Tremel, *Adv. Funct. Mater.* **2020**, *31*, 2007830. https://doi.org/10.1002/adfm.202007830
29. C. M. Zaremba, D. E. Morse, S. Mann, P. K. Hansma, G. D. Stucky, *Chem. Mater.* **1998**, *10*, 3813. https://doi.org/10.1021/cm970785g
30. M. Wang, R. Qian, M. Bao, C. Gu, P. Zhu. *Mater. Lett.*, **2018**, *210*, 203. https://doi.org/10.1016/j.matlet.2017.09.023
31. L. O. Filippov, I. V. Filippova, O. B. Kaba, D. Fornasiero, *Miner. Eng.* **2021**, *162*, 106729. https://doi.org/10.1016/j.mineng.2020.106729
32. E. Szarawara, B. Trybalska, M. Cichocin, A. Stoch, W. Jastrze, A. Broz, *J. Mol. Struct.* **1999**, *512*, 287.
33. A. Grunenwald, C. Keyser, A. M. Sautereau, E. Crubézy, B. Ludes, C. Drouet, *J. Archaeol. Sci.* **2014**, *49*, 134. https://doi.org/10.1016/j.jas.2014.05.004
34. R. Narayanan, S. K. Seshadri, T. Y. Kwon, K. H. Kim, *J. Biomed. Mater. Res. Part B Appl. Biomater.* **2008**, *85*, 279. https://doi.org/10.1002/jbm.b.30932
35. S. C. Liou, S. Y. Chen, H. Y. Lee, J. S. Bow, *Biomaterials* **2004**, *25*, 189. https://doi.org/10.1016/S0142-9612(03)00479-4
36. F. H. Y. Lui, R. J. Mobbs, Y. Wang, P. Koshy, F. Lucien, D. Zhou, C. C. Sorrell, *Adv. Mater. Interfaces*. **2021**, *8*, 2100333.
37. C. Lc, *Dent. Mater. J.* **2009**, *28*, 1.
38. M. Ni, B. D. Ratner, *Biomaterials* **2003**, *24*, 4323. https://doi.org/10.1016/S0142-9612(03)00236-9
39. T. Hasegawa, T. Yamamoto, E. Tsuchiya, H. Hongo, K. Tsuboi, A. Kudo, M. Abe, T. Yoshida, T. Nagai, N. Khadiza, A. Yokoyama, K. Oda, H. Ozawa, P. H. L. de Freitas, M. Li, N. Amizuka, *Jpn. Dent. Sci. Rev.* **2017**, *53*, 34. https://doi.org/10.1016/j.jdsr.2016.09.002
40. L. Yan, D. M. Jiang, *Devel. Ther.* **2015**, *9*, 6497. https://doi.org/10.2147/DDDT.S96207

41. T. A. Franz-Odendaal, B. K. Hall, P. E. Witten, *Dev. Dyn.* **2006**, *235*, 176. https://doi.org/10.1002/dvdy.20603
42. A. Akiva, J. Melke, S. Ansari, N. Liv, R. van der Meijden, M. van Erp, F. Zhao, M. Stout, W. H. Nijhuis, C. de Heus, C. Muñiz Ortera, J. Fermie, J. Klumperman, K. Ito, N. Sommerdijk, S. Hofmann, *Adv. Funct. Mater.* **2021**, *31*, 2010524. https://doi.org/10.1002/adfm.202010524
43. S. Chen, X. Shi, H. Morita, J. Li, N. Ogawa, T. Ikoma, S. Hayakawa, Y. Shirosaki, A. Osaka, N. Hanagata, *Sci. Technol. Adv. Mater.* **2011**, *12*. https://doi.org/10.1088/1468-6996/12/6/065003
44. L. F. Fernandes, M. A. Costa, M. H. Fernandes, H. Tomás. *Connect. Tissue Res.* **2009**, *50*, 336. https://doi.org/10.1080/03008200902855909
45. Z. Xiao, C. E. Camalier, K. Nagashima, K. C. Chan, D. A. Lucas, M. J. D. E. L. A. Cruz, M. Gignac, S. Lockett, H. J. Issaq, T. D. Veenstra, T. P. Conrads, G. R. Beck, *J. Cell. Physiol.* **2007**, *335*, 325. https://doi.org/10.1002/jcp
46. Z. Xiao, C. E. Camalier, K. Nagashima, K. C. Chan, D. A. Lucas, M. J. De La Cruz, M. Gignac, S. Lockett, H. J. Issaq, T. D. Veenstra, T. P. Conrads, G. R. Beck, *J. Cellular Physiol.* **2007**, *210*, 325. https://doi.org/10.1002/jcp.20826
47. Y. Chen, A. George. *Front. Physiol.* **2018**, *9*, 1. https://doi.org/10.3389/fphys.2018.01092
48. C. C. Chua, B. H. L. Chua, Z. Chen, C. Landy, R. C. Hamdy. *Biochim. Biophys. Acta* **2003**, *1642*, 79. https://doi.org/10.1016/S0167-4889(03)00100-9
49. P. Lagonegro, G. Trevisi, L. Nasi, L. Parisi, E. Manfredi, S. Lumetti, F. Rossi, G. M. Macaluso, G. Salviati, C. Galli, *Dent. Mater. J.* **2018**, *37*, 278. https://doi.org/10.4012/dmj.2017-008
50. C. Morris, J. Thorpe, L. Ambrosio, M. Santin, *J. Nutr.* **2006**, *136*, 1166. https://doi.org/10.1093/jn/136.5.1166
51. T. Yamaguchi, *J. Bone Miner. Metab.* **2008**, *26*, 301. https://doi.org/10.1007/s00774-008-0843-7
52. S. L. Godwin, S. P. Soltoff, *J. Biol. Chem.* **1997**, *272*, 11307. https://doi.org/10.1074/jbc.272.17.11307
53. T. Yamaguchi, N. Chattopadhyay, O. Kifor, R. R. Butters, T. Sugimoto, E. M. Brown, *J. Bone Miner. Res.* **1998**, *13*, 1530. https://doi.org/10.1359/jbmr.1998.13.10.1530
54. T. Yamaguchi, N. Chattopadhyay, O. Kifor, C. Ye, P. M. Vassilev, J. L. Sanders, E. M. Brown, *Am. J. Physiol. Cell Physiol.* **2001**, *280*, 382. https://doi.org/10.1152/ajpcell.2001.280.2.c382
55. M. M. Dvorak, D. Riccardi, *Cell Calcium* **2004**, *35*, 249. https://doi.org/10.1016/j.ceca.2003.10.014
56. A. Guan, P. Hamilton, Y. Wang, M. Gorbet, Z. Li, K. S. Phillips, *Nat. Biomed. Eng.* **2017**, *1*, 1. https://doi.org/10.1038/s41551-017-0045

SUPPORTING INFORMATION

Additional supporting information can be found online in the Supporting Information section at the end of this article.

How to cite this article: Florence H.Y. Lui, Liangcheng Xu, Pierrette Michaux, Joanna Biazik, Gregory F.S. Harm, Rema A. Oliver, Pramod Koshy,William R. Walsh, Ralph J. Mobbs, Tara C. Brennan-Speranza, Yu Wang, Lidan You, Charles C. Sorrell. *Nano Select*. **2022**, 1. https://doi.org/10.1002/nano.202200102.